

Analytical Modeling of Transient Electromigration Stress based on Boundary Reflections

Mohammad Abdullah Al Shohel¹, Vidya A. Chhabria¹, Nestor Evmorfopoulos², and Sachin S. Sapatnekar¹
¹ University of Minnesota, Minneapolis, MN 55455 ² University of Thessaly, Volos, Greece

Abstract—Traditional methods that test for electromigration (EM) failure in multisegment interconnects, over the lifespan of an IC, are based on the use of the Blech criterion, followed by Black’s equation. Such methods analyze each segment independently, but are well known to be inaccurate due to stress buildup over multiple segments. This paper introduces the new concept of boundary reflections of stress flow that ascribes a physical (wave-like) interpretation to the transient stress behavior in a finite multisegment line. This can provide a framework for deriving analytical expressions of transient EM stress for lines with any number of segments, which can also be tailored to include the appropriate number of terms for any desired level of accuracy. The proposed method is shown to have excellent accuracy, through evaluations against the FEM solver COMSOL, as well as scalability, through its application on large power grid benchmarks.

I. INTRODUCTION

Electromigration (EM) in on-chip interconnects is a major source of concern in both digital and analog circuits in deeply scaled technologies. EM concerns arise especially in interconnects that carry large currents, e.g., power grid wires in digital and analog circuits, or wires carrying large biasing currents in analog circuits. EM failures are related to the current densities in wires: as wires have grown narrower in recent technologies, these current densities have increasingly resulted in EM susceptibility in lower metal layers.

Traditional EM analysis methods have been largely empirical. A widely used approach employs the Blech product [1] to first identify “immortal” wires, after which a method based on Black’s equation [2] tests the current density in potentially mortal wires against foundry-specified thresholds. However, there is a growing realization that such empirical methods can lead to incorrect conclusions, and that EM in multisegment interconnects requires a physics-based analysis that is more complex. Following the work in [3]–[5], a significant advance in modeling in Korhonen [6] presents a differential equation formulation for each wire segment, modeling the interplay between the electron wind force, driven by the current density, and the opposing back stress force, driven by the diffusion gradient cause by imbalanced accumulation of metal atoms as they migrate along a wire.

This system of differential equations can be solved to obtain the stress in each wire segment. Two types of analysis are useful. *Steady-state* analysis predicts the largest EM-induced stress in any wire segment after all transients settle: if this stress is below the critical stress for void formation, the wire segment can be considered immortal. However, the time required to reach steady-state may often exceed the useful lifetime of a chip. For such scenarios, a *transient analysis* predicts the stress as a function of time, and a wire is EM-susceptible if its stress exceeds the critical stress during its lifetime. Several approaches have used the Korhonen formulation [7], [8]. For multisegment metal interconnects, analyses based on *steady-state* stress [9]–[12] are used to identify immortal wires in multisegment wires: this problem was recently shown to admit a linear-time solution [12]. The problem of analyzing *transient* stress to determine the stress at the end-of-lifetime period for the chip has seen several

prior attempts, but is computationally expensive. Previous work in [13], [14] first finds the infinite series solution and then truncates it to a suitable number of terms. However, using this approach (a) it is very difficult to calculate and write down the infinite series for more than 3-4 segments; (b) it is practically impossible to obtain expressions parameterized by a general number of segments; (c) it is difficult to know how many terms the series should be truncated to while maintaining sufficient accuracy. In [15], a numerical solution for transient analysis is described.

In this paper, we consider the problem of finding a closed-form solution to the transient stress profile in a multisegment metal interconnect line due to EM. The reasoning behind limiting our focus to only line structures is presented in Section III-A. Our contributions are summarized as follows. *First*, our approach introduces the new concept of boundary reflections of stress flow, which ascribes a physical interpretation to the transient EM stress behavior and provides insight to the terms of the infinite series solution. *Second*, our proposed approach can, for the first time, provide analytic solutions of transient stress for multisegment lines with an arbitrary number of segments (i.e., not just restricted to lines with 3-4 segments), which can be also parameterized with respect to the number of segments. The proposed framework starts from the sources of stress flow (to be defined later) as fundamental terms and builds up the series solution by successive reflections at the physical boundaries. We provide general expressions for the fundamentals and the first group of reflections as function of the number and length of segments in easy-to-use tabular forms, from which the analytic solution containing an arbitrary number of reflections (or even the full infinite series solution) can be easily deduced. *Third*, based on our physical explanation, the framework provides a concrete termination criterion that can be customized to each stress source: based on the fact that the reflections of subsequent orders attenuate, we can stop the build-up of the series at any desired accuracy. It is seen experimentally that at most two reflections for each stress source are sufficient for near-perfect accuracy for all of our testcases until we reach steady-state. In addition, the capability for computation of transient stress in any multisegment line allows the application of the proposed method to very large chip structures such as power grids. This is the first work to show an analytic method that is applicable to structures of this scale, and our experiments on large power grid benchmarks demonstrate significant pessimism of steady state predictions vs. the actual EM failures at the end of chip lifetime.

Next, after providing basic background on EM analysis in Section II, we present our analytical modeling framework in Section III. Finally, in Section IV, we present an evaluation of our approach on a set of test cases, and we conclude the paper in Section V.

II. BACKGROUND

Fig. 1 shows the cross-section of a Cu dual-damascene (DD) wire and illustrates the electromigration mechanism in terms of two driving forces i.e. the electron wind force and the back-stress force. When current flows in the wire, the momentum of the electrons drive metal atoms from the cathode towards the anode, in the direction of electron flow. Due to this electron wind force, the cathode gets

This work was supported in part by the NSF under award CCF-1714805 and by the DARPA IDEA program, and by the Louise Dossdall Fellowship. The work of the third author was supported in part by a Scholar grant from the Fulbright Foundation, Greece.

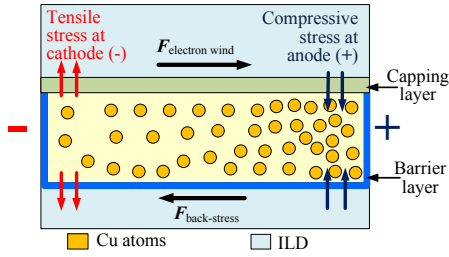


Figure 1: Illustration of electromigration in a Cu wire [10].

depleted of metal atoms that may lead to void formation, resulting in open circuits. The movement of migrating atoms is limited to a single metal layer since the barrier layer acts as a blocking boundary for mass transport [16], [17] and prevents atoms from migrating to other metal layers. As a result, mass depletion of atoms occurs at the cathode terminal and a tensile stress gets built up near the cathode. Simultaneously, migrating atoms get accumulated at the anode terminal and a compressive stress is created near the anode. As metal atoms migrate towards the anode, the resulting concentration gradient creates a stress-induced reverse flow of atoms to the cathode. This force, which acts against the electron wind force, is proportional to the stress gradient and known as back-stress force.

A single interconnect segment injects electron current at a cathode at $x = 0$ towards an anode at $x = L$. The temporal evolution of EM-induced stress, $\sigma(x, t)$, at any point in the segment is modeled by the partial differential equation [6]:

$$\frac{\partial \sigma}{\partial t} = \frac{\partial}{\partial x} \left[\kappa \left(\frac{\partial \sigma}{\partial x} + G \right) \right] \quad (1)$$

Here, $G = j(Z^* e \rho) / \Omega$, and $\kappa = D_a \mathcal{B} \Omega / (kT)$, where j is the current density through the wire, Z^* is the effective charge number, e is the electron charge, ρ is the resistivity, Ω is the atomic volume for the metal, \mathcal{B} is the bulk modulus of the material, k is Boltzmann's constant, T is the temperature, and $D_a = D_0 e^{-E_a/kT}$ is the diffusion coefficient, with E_a being the activation energy.

In the absence of current flow, the only stress in the wire is the thermally-induced stress, σ_T , that originates due to differentials in the coefficient of thermal expansion (CTE) in the interconnect materials. The differential equation with the boundary conditions can be solved numerically to obtain the transient behavior of stress over time and then applying superposition principle σ_T can be added to account for CTE effects. The impact of σ_T is realized by offsetting the critical stress, σ_{crit} , to $(\sigma_{crit} - \sigma_T)$.

As in [6], the sign convention for j is in the direction of electron current, i.e., opposite to conventional current and the electric field. There are two terms on the right hand side of (1). The second term that contains G represents atomic flux attributable to the electron wind force, while the first term containing the stress gradient $\frac{\partial \sigma}{\partial x}$ accounts for the flux related to the back-stress force. The sum, $(\partial \sigma / \partial x + G)$, is proportional to the net atomic flux. The constant of proportionality varies linearly with the wire cross-sectional area.

BCs for single-segment interconnect When electron current is injected through the anode and flows to the cathode at the other end, we have zero-flux conditions at each end:

$$\frac{\partial \sigma}{\partial x} + G = 0 \quad \forall t \text{ at } x = 0, x = L. \quad (2)$$

BCs for a multisegment interconnect line In an N -segment interconnect line, shown in Fig. 2, currents may be injected (or drawn) at intermediate points through vias (recall that atomic flux does not cross vias in Cu DD designs), and the currents in each segment may be unequal.



Figure 2: A multisegment interconnect line with potentially nonuniform segment lengths, showing the G value in each segment.

At $x = 0$ and $x = L_N$ the boundary conditions dictate that there is zero atomic flux through the boundaries at the end points over all time, i.e.,

$$\frac{\partial \sigma_1}{\partial x} \Big|_{x=0} + G_1 = 0; \quad \frac{\partial \sigma_N}{\partial x} \Big|_{x=L_N} + G_N = 0 \quad (3)$$

At intermediate nodes, the boundary conditions state that the atomic flux entering each boundary must be zero. For $i = 1, \dots, N-1$ [11],

$$\left(\frac{\partial \sigma_i}{\partial x} \Big|_{x=L_i} + G_i \right) = \left(\frac{\partial \sigma_{i+1}}{\partial x} \Big|_{x=L_i} + G_{i+1} \right) \quad (4)$$

Moreover, the stress must be continuous at each intermediate node, leading to the boundary condition:

$$\sigma_i \Big|_{x=L_i} = \sigma_{i+1} \Big|_{x=L_i} \quad (5)$$

III. ANALYTICAL MODELING OF TRANSIENT STRESS VIA STRESS FLOWS AND REFLECTIONS

We begin by justifying the importance of analyzing line structures in modern designs. We then provide analytical solutions for stress, first for a single-segment line (Section III-B), then for a two-segment line (Section III-C), and finally, generalized to multiple segments (Section III-D). The details of the supporting derivations, which are based on the method of Laplace transformation, are provided in the Appendix so as not to interrupt the flow of the paper. For the first two cases, we present the solution as an infinite sum and examine each term to obtain an intuitive understanding of the expressions. We use this insight to extend the framework to multisegment lines, and also to develop truncation criteria for the infinite sum based on an accuracy specification.

A. Why is it enough to analyze line structures?

In scaled FinFET technologies using Cu DD interconnects, interconnect lines typically adhere to a set of requirements imposed by lithographic constraints and design methodologies:

- 1) As stated above, all mass transfer occurs within each metal layer as migrating atoms are prevented from moving across vias across metal layers due to blocking boundaries in Cu DD interconnects [16], [17].
- 2) Lithography considerations dictate that especially in lower metal layers (which are now seen to be susceptible to electromigration [18]), wires must be routed unidirectionally. As a result, all wires in a given layer are oriented in the same direction, and lines are the most commonly encountered structures.
- 3) In principle, bidirectional routing and meshes could be used in upper metal layers that are less constrained by lithography. However, to facilitate routing of signal/clock wires, design methodologies widely use unidirectional routes and create meshes by connecting grids of parallel orthogonal wires in successive layers [19]–[21]. Thus, in each layer, separated from neighboring layers by blocking boundaries, the resulting structure is a line.

Thus, for modern chips, it is sufficient to consider the analysis of the line structures analyzed in this work. In some instances, very short leads (“stubs”) may be introduced to connect the line to vias, but these short stubs are unlikely to impact the solution. The steady-state stress across these stubs is proportional to the product of their current density j times length l : considering the steady-state as an upper bound, the small (jl) product for the stubs implies that their stress impact on the line is negligible in practice.

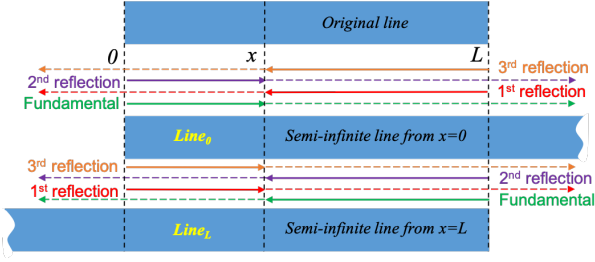


Figure 3: A single-segment wire illustrating fundamental and first two reflections of stress flow originating at side boundaries.

B. Single-segment line

At location x on a semi-infinite line starting at $x = 0$, at time t , the solution to the stress equation is derived in the Appendix as (24) as:

$$\sigma(x, t) = G \cdot g(x, t) \quad (6)$$

where

$$g(X, t) = 2\sqrt{\frac{\kappa t}{\pi}} \exp\left(-\frac{X^2}{4\kappa t}\right) - X \operatorname{erfc}\left(\frac{X}{2\sqrt{\kappa t}}\right) \quad (7)$$

$\operatorname{erfc}(x) = \frac{2}{\sqrt{\pi}} \int_x^\infty e^{-t^2} dt$ is the complementary error function. This expression is identical to that provided in [6]. Similarly, for a line starting at $x = L$ and extending to $-\infty$, the Appendix shows (eq. (26)) that the stress can be written as

$$\sigma(x, t) = -G \cdot g(L - x, t) \quad (8)$$

where $g(\cdot)$ is as defined in (7).

For a single-segment interconnect line of length L carrying a constant current density, j , the Appendix shows (eq. (28)) that the solution to the stress equation is:

$$\sigma(x, t) = G \sum_{n=0}^{\infty} (-1)^n [g(nL + x, t) - g((n+1)L - x, t)] \quad (9)$$

Based on the resemblance between Equations (6) and (9), we can construct a physical interpretation for the elements of the infinite summation. This is illustrated in Fig. 3, which shows the single-segment line on top and its decomposition into two semi-infinite lines. As we will show below, the stress profile at location x on the line corresponds to a superposition of the stresses in the two semi-infinite lines, where $n = 0$ corresponds to the fundamental mode; every other value of n corresponds to a “stress wave”¹ that is reflected n times. **$\underline{n} = 0$:** This *fundamental* term consists of the terms $G \cdot g(x, t)$ and $-G \cdot g(L - x, t)$ which can easily be seen to correspond to superposition of (a) the stress at x in a semi-infinite line from 0 to ∞ (denoted as $Line_0$), where the distance from the left edge is x , and (b) the stress at x in a semi-infinite line from L to $-\infty$ (denoted as $Line_L$), where the distance traveled from the right edge is $L - x$. This is illustrated by the fundamental mode shown in Fig. 3, shown by the green arrows next to $Line_0$ and $Line_L$. In view of the boundary conditions (2), these terms have the physical interpretation of two sources of stress flow equal to $\partial\sigma/\partial x = -G$ originating at the two boundaries (at $x = 0$ and $x = L$) and traveling down in semi-infinite lines of opposite directions.

$\underline{n} = 1$: Using a similar argument, the two terms $G \cdot g(2L - x, t)$ and $-G \cdot g(L + x, t)$ can be regarded as *reflections* of the aforementioned stress flows at the opposite boundaries, which are then superposed to the original fundamental components. Specifically, the term $G \cdot g(2L - x, t)$ is the stress flow originating at $x = 0$ on $Line_0$ after being reflected at L and going back at x (traveling total distance $L + (L - x) = 2L - x$), while $-G \cdot g(L + x, t)$ represents the stress

¹Although stress is by no means a wave but a diffusing quantity governed by equation (1), we informally call it a stress wave to emphasize the property of reflection that it shares with waves and which is central to our development.

Table I: Stress flow components in a single-segment wire

Source of stress flow	Component	Distance X traveled
Left Boundary $x = 0$	Fundamental	x
	1 st Reflection	$2L - x$
	2 nd Reflection	$2L + x$
	3 rd Reflection	$4L - x$
Right Boundary $x = L$	Fundamental	$L - x$
	1 st Reflection	$L + x$
	2 nd Reflection	$3L - x$
	3 rd Reflection	$3L + x$

flow originating at $x = L$ on $Line_L$ after being reflected at $x = 0$ and going back at x (traveling total distance $L + x$). Fig. 3 illustrates the first reflection to point x on $Line_0$ and $Line_L$.

$\underline{n} = 2$: Here, the term $G \cdot g(2L + x, t)$ is the stress flow from $x = 0$ on $Line_0$ after two reflections (at $x = L$ and then at $x = 0$) before traveling to location x (having traveled distance $2L + x$). Likewise, $-G \cdot g(L + x, t)$ is the stress flow from $x = L$ on $Line_L$ after reflections at $x = 0$ and then $x = L$ before going back to location x (having traveled distance $2L + (L - x) = 3L - x$). The second and third reflections for $Line_0$ and $Line_L$ are shown in Fig. 3.

The reflected components reach the point x attenuated (being equal to a fundamental that has traveled longer and longer distances) and their contribution diminishes with each subsequent reflection. The fundamental terms as well as the first three reflections of stress flow for the single-segment wire are summarized in Table I.

C. Two-segment line

A two-segment line, shown in Fig. 4 can be considered to consist of two line segments, one from $x = 0$ to $x = L_1$, with parameter G_1 , and another from $x = L_1$ to $x = L_2$ with parameter G_2 , where G_1 and G_2 depend on the current densities in the two segments. The line consists of stress flow discontinuities at the ends of each segment, i.e., $x = 0$ and $x = L_2$, both similar to the single-segment line. At $x = L_1$, the lines must obey boundary conditions that enforce the continuity of atomic flux (4), and continuity of stress (5).

The discontinuities at $x = 0$ and $x = L_2$ are handled in a similar way as the single-segment line, by considering semi-infinite lines that originate at those points. At $x = L_1$, the boundary condition (4) indicates that there is another source of stress flow due to the discontinuity² $\frac{\partial\sigma_1}{\partial x} - \frac{\partial\sigma_2}{\partial x} = G_2 - G_1$ at the intersection point. This source creates two fundamental components that travel sideways from $x = L_1$ and along the semi-infinite parts of a two-segment infinite line $(-\infty < x < L_1) \wedge (L_1 < x < +\infty)$ (denoted as $Line_{L_1}$). The Appendix shows (eqs. (32)) that the fundamental traveling left (for $x < L_1$) is $\frac{G_2 - G_1}{2} g(L_1 - x, t)$, while the fundamental traveling right (for $x > L_1$) is $\frac{G_2 - G_1}{2} g(x - L_1, t)$.

The fundamentals due to the discontinuity at the intersection are superposed to the fundamentals of stress flow originating at the boundaries $x = 0$ and $x = L_2$, as shown in Fig. 4. Like the fundamentals originating at the boundaries, the fundamentals originating at $x = L_1$ are also reflected at the boundaries $x = 0$ and $x = L_2$. Specifically,

- The leftward traveling fundamental undergoes a 1st reflection at $x = 0$ before arriving (again or for the first time) at location x (having traveled distance $L_1 + x$), then a 2nd reflection at the boundary $x = L_2$ before arriving once again at x (with distance traveled $L_1 + L_2 + (L_2 - x) = L_1 + 2L_2 - x$), and so on.
- The rightward traveling fundamental undergoes a 1st reflection at $x = L_2$ before arriving (again or for the first time) at location x (having traveled distance $(L_2 - L_1) + (L_2 - x) = -L_1 + 2L_2 -$

²This is analogous to the electrostatic case of a surface charge being a source of electric potential gradient (i.e. electric field) through the discontinuity of the normal derivative.

x), then a 2nd reflection at $x = 0$ before arriving once again at x (with distance traveled $(L_2 - L_1) + L_2 + x = -L_1 + 2L_2 + x$), and so on.

The fundamental terms as well as the first four reflections of all sources of stress flow for the two-segment wire are summarized in Table II. Regarding the stress flow from the intersection, we note that depending on the location of the variable point x relative to the intersection point $x = L_1$ only one fundamental contributes before the reflections commence (leftward traveling fundamental for $x < L_1$ and rightward traveling fundamental for $x > L_1$), while all reflections of both fundamentals arrive afterwards at x .

Generalizing the traveling distances from the table, we can write infinite series expressions for the stress due to the flow from the left boundary (LB) and the right boundary (RB) as:

$$\sigma^{LB}(x, t) = G_1 \sum_{n=0}^{\infty} [g(2nL_2 + x, t) + g((2n+2)L_2 - x, t)] \quad (10)$$

$$\sigma^{RB}(x, t) = -G_2 \sum_{n=0}^{\infty} [g((2n+1)L_2 - x, t) + g((2n+1)L_2 + x, t)] \quad (11)$$

Similarly, excluding the fundamentals, the infinite series expressions for the stress flow from the intersection traveling to the left (IL) and to the right (IR) are:

$$\sigma^{IL}(x, t) = \frac{G_2 - G_1}{2} \sum_{n=0}^{\infty} [g(L_1 + 2nL_2 + x, t) + g(L_1 + (2n+2)L_2 - x, t)] \quad (12)$$

$$\sigma^{IR}(x, t) = \frac{G_2 - G_1}{2} \sum_{n=0}^{\infty} [g(-L_1 + (2n+2)L_2 - x, t) + g(-L_1 + (2n+2)L_2 + x, t)] \quad (13)$$

The infinite series (10) to (13) are superposed with each other, and with the addition of the proper (left or right) fundamental from the intersection, yield the final stresses in the areas $0 < x < L_1$ and $L_1 < x < L_2$, respectively, as:

$$\sigma_1(x, t) = \sigma^{LB}(x, t) + \sigma^{RB}(x, t) + \sigma^{IL}(x, t) + \frac{G_2 - G_1}{2} g(L_1 - x, t) + \sigma^{IR}(x, t) \quad (14)$$

$$\sigma_2(x, t) = \sigma^{LB}(x, t) + \sigma^{RB}(x, t) + \sigma^{IL}(x, t) + \frac{G_2 - G_1}{2} g(x - L_1, t) + \sigma^{IR}(x, t) \quad (15)$$

It can be verified that, accounting for the difference in coordinate systems, the series (14, 15) exactly match the infinite series solution that has been laboriously calculated in [13], [14]. Unlike our approach where each term has a physical interpretation, the expressions in that work do not provide specific insights into the solution.

The benefits of our approach building up the series solution by stress flow fundamentals and reflections (instead of calculating first the infinite series and then truncating the number of terms) are:

- The approach can be effortlessly extended to a larger (and general) number of segments (as described in Section III-D).
- The series build-up can be terminated at any point and with prescribed accuracy (while the accuracy of truncation of an infinite series cannot be determined beforehand, and usually keeping only the term $n = 0$ results in poor accuracy). Section III-E discusses the formulation of an appropriate termination criterion.

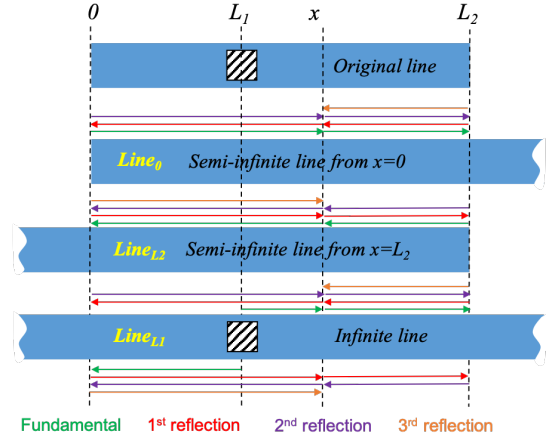


Figure 4: A 2-segment wire illustrating fundamental and first two reflection components of stress flow originating from the side boundaries at $x = 0$ and $x = L_2$, and from the intersection at $x = L_1$.

Table II: Stress flow components in a two-segment line

Source of stress flow	Component	Distance X traveled
Left Boundary, $x = 0$	Fundamental	x
	1 st reflection	$2L_2 - x$
	2 nd reflection	$2L_2 + x$
	3 rd reflection	$4L_2 - x$
	4 th reflection	$4L_2 + x$
Right Boundary, $x = L_2$	Fundamental	$L_2 - x$
	1 st reflection	$L_2 + x$
	2 nd reflection	$3L_2 - x$
	3 rd reflection	$3L_2 + x$
	4 th reflection	$5L_2 - x$
Intersection, $x = L_1$, to the left	Fundamental	$L_1 - x$ if $x < L_1$; else none
	1 st reflection	$L_1 + x$
	2 nd reflection	$L_1 + 2L_2 - x$
	3 rd reflection	$L_1 + 2L_2 + x$
	4 th reflection	$L_1 + 4L_2 - x$
Intersection $x = L_1$, to the right	Fundamental	$x - L_1$ if $x > L_1$; else none
	1 st reflection	$-L_1 + 2L_2 - x$
	2 nd reflection	$-L_1 + 2L_2 + x$
	3 rd reflection	$-L_1 + 4L_2 - x$
	4 th reflection	$-L_1 + 4L_2 + x$

D. Multisegment line

A multisegment line of length L_N , illustrated in Fig. 5, is composed of N line segments with parameters G_1 to G_N (corresponding to different current densities) and intersection points at locations $x = L_1$ to $x = L_{N-1}$ (where the length of the k^{th} -segment is $L_k - L_{k-1}$). The stress in every segment is governed by Korhonen's equation (1), and the boundary conditions of continuity of atomic flux (4) and continuity of stress (5) must be satisfied at the intersection points.

The analytical solution of stress for the N -segment wire entails symbolically solving (in the Laplace or s -domain) N differential equations that are coupled by $2N$ boundary conditions, and then transforming the solutions back to the time domain via inverse transforms. This involves very heavy algebra for $N \geq 3$ and expressions which are extremely long to even write down (and impossible to do so for general N). The approach of building up the series solution by stress flow fundamentals and reflections, which was described for the two-segment wire in Section III-C, provides a natural extension framework for any number of segments N . In particular, one has only to consider the fundamental components of stress flow from the two boundaries $x = 0$, $x = L_N$ and the $N - 1$ intersection points, along with a limited number of reflections of these components at the

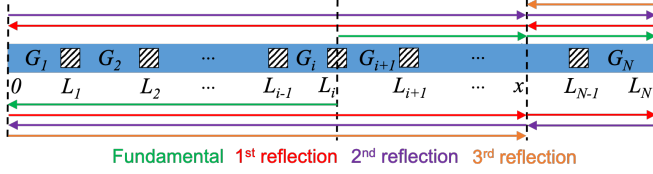


Figure 5: A N -segment wire illustrating fundamental and first two reflections of stress flow originating at an intermediate junction.

Table III: Stress flow components in an N -segment line

Source of stress flow	Component	Distance X traveled
Left Boundary $x = 0$	Fundamental	x
	1 st reflection	$2L_N - x$
	2 nd reflection	$2L_N + x$
	3 rd reflection	$4L_N - x$
	4 th reflection	$4L_N + x$
Right Boundary $x = L_N$	Fundamental	$L_N - x$
	1 st reflection	$L_N + x$
	2 st reflection	$3L_N - x$
	3 rd reflection	$3L_N + x$
	4 th reflection	$5L_N - x$
Intersection $x = L_i$ ($i = 1, \dots, N-1$), to the left	Fundamental	$L_i - x$ if $x < L_i$; else none
	1 st reflection	$L_i + x$
	2 nd reflection	$L_i + 2L_N - x$
	3 rd reflection	$L_i + 2L_N + x$
	4 th reflection	$L_i + 4L_N - x$
Intersection $x = L_i$ ($i = 1, \dots, N-1$), to the right	Fundamental	$x - L_i$ if $x > L_i$; else none
	1 st reflection	$-L_i + 2L_N - x$
	2 nd reflection	$-L_i + 2L_N + x$
	3 rd reflection	$-L_i + 4L_N - x$
	4 th reflection	$-L_i + 4L_N + x$

boundaries (reflections of subsequent orders die out fast, as argued in Section III-E). Table III lists the fundamentals and the first four reflections of all sources of stress flow in the N -segment wire.

In fact, generalizing the distances from the table, it is perfectly possible to write the full infinite series solution for the multisegment wire with a general number of segments N (which has not been possible thus far). The series will be like (14, 15) but with a sum over all $N-1$ intersections. However, since infinite series are not very useful for practical computations, we write here the analytical expression containing the fundamentals and two reflections for each source (which suffice to provide near-perfect accuracy for times up to steady-state in all cases that were evaluated experimentally). This constitutes the first analytical expression that gives transient stress in every point of the N -segment wire for arbitrary values of N :

$$\begin{aligned}
\sigma(x, t) \approx & G_1 [g(x, t) + g(2L_N - x, t) + g(2L_N + x, t)] \\
& - G_N [g(L_N - x, t) + g(L_N + x, t) + g(3L_N - x, t)] \\
& + \sum_{i=1}^{N-1} \frac{G_{i+1} - G_i}{2} [g(|L_i - x|, t) + g(L_i + x, t) \\
& + g(L_i + 2L_N - x, t) + g(-L_i + 2L_N - x, t) \\
& + g(-L_i + 2L_N + x, t)] \quad (16)
\end{aligned}$$

where $g(\cdot)$ is the function defined in (7). The above expression can easily be adapted to include more (or fewer) reflected terms (and even different number of reflected terms for each individual source), and Section III-E formulates appropriate criteria for termination of the series build-up subject to a desired level of accuracy.

E. Defining Terminating Criteria

In this section, we present criteria for truncating each infinite series component of the solution, such as (14) and (15). In fact, separate

termination criteria can be found for each source of stress – the left edge ($x = 0$), the right edge ($x = L_N$), or any intermediate discontinuity ($x = L_i, 1 \leq i < N$), using the ideas presented below.

For any such source (e.g., the source at the left, modeled by (6)), the fundamental is the dominant component of stress flow, and the higher order reflection terms diminish quickly since the function $g(\cdot)$ decays exponentially with distance traveled. Let us consider that the first k reflections up to k^{th} -order are good enough to reach reasonable accuracy. This translates to:

$$\sigma(x, t) \approx \sigma^{(0)}(x, t) + \sigma^{(1)}(x, t) + \dots + \sigma^{(k)}(x, t) \quad (17)$$

where $\sigma^{(0)}(x, t)$ is the fundamental and $\sigma^{(k)}(x, t)$ is the k^{th} -order reflection.

For a stress source at $x_L \in \{0, L_1, L_2, \dots, L_N\}$ and a reflection at an edge $x_E \in \{0, L_N\}$, we set the termination criterion to

$$|\sigma^{(k+1)}(x_E, t)| < \alpha |\sigma^{(0)}(x_L, t)|, \quad (18)$$

where α is given and controls the tolerance. Since the stress wave attenuates exponentially with distance, this indicates that the contribution of the $k+1^{\text{th}}$ -order reflection is not significant, so that the infinite series can be truncated at k^{th} -order reflection.

Note that the impact of each stress source can be considered independently, and our method provides the flexibility of choosing a different number of terms for each stress source. For instance, if $G_i - G_{i+1}$ is relatively small, then the impact of the corresponding stress discontinuity at $x = L_i$ may be small and the summation for $g(\cdot)$ can be truncated early. Note that this flexibility and insight is unavailable in conventional truncation of infinite series (e.g., in [14]), which truncates all sources after the same number of terms.

IV. RESULTS

We present two sets of results to illustrate the accuracy and scalability of our boundary reflection based approach. Section IV-A demonstrates our methodology and shows comparisons of our approach with a FEM based numerical solver, COMSOL, for a five-segment Cu DD line. Then, in Section IV-B we employ our algorithm on large power grid benchmarks. Our analysis of power grids on designs synthesized on 12nm and 28nm (both commercial) PDKs, and on the Nangate 45nm PDK (all based on Cu DD interconnects) illustrates the risk of EM-failure in modern VLSI designs.

The Cu DD interconnect specifications used in all our simulations are [8], [22]: $Z^* = 1$, $e = 1.6 \times 10^{-19}$ C, $\rho = 2.25 \times 10^{-8}$ Ω m, $\mathcal{B} = 28$ GPa, $\Omega = 1.18 \times 10^{-29}$ m³, $D_0 = 1.3 \times 10^{-9}$ m²/s, $k = 1.38 \times 10^{-23}$ J/K, $T = 378$ K, and $\sigma_{crit} = 41$ MPa.

A. Comparison with COMSOL on a multi-segment line

We illustrate the application of our approach on a five-segment line with uneven segment lengths of (from left to right) 20 μ m, 25 μ m, 15 μ m, 10 μ m, and 30 μ m. The corresponding current densities are -2×10^{10} A/m², 1×10^{10} A/m², 1.5×10^{10} A/m², -1×10^{10} A/m², and 0.5×10^{10} A/m², respectively. Prior analytical solutions for straight lines have limited their results to two-segment cases as the analytical formulas become much more complex beyond two segments.

As time passes, we expect more reflections to come into play, and we show the components of transient stress build-up at $t = 6.3e8$ s, or 20 years in Fig. 6. This period is at the high end of product lifetime, typically used for automotive applications, and we choose it to provide a sense of the number of reflections that are required by our method. The figure shows the stress components generated from each of the stress sources: from the side boundaries, $x = 0$ and $x = L_5$ in (a) and (f), respectively, and from the intersection points at $x = L_1$ through L_4 in (b)–(e). It can be visually seen that the first reflections in (a) and (f) are significantly attenuated with respect to the fundamentals, and the magnitude of stress at the second reflection

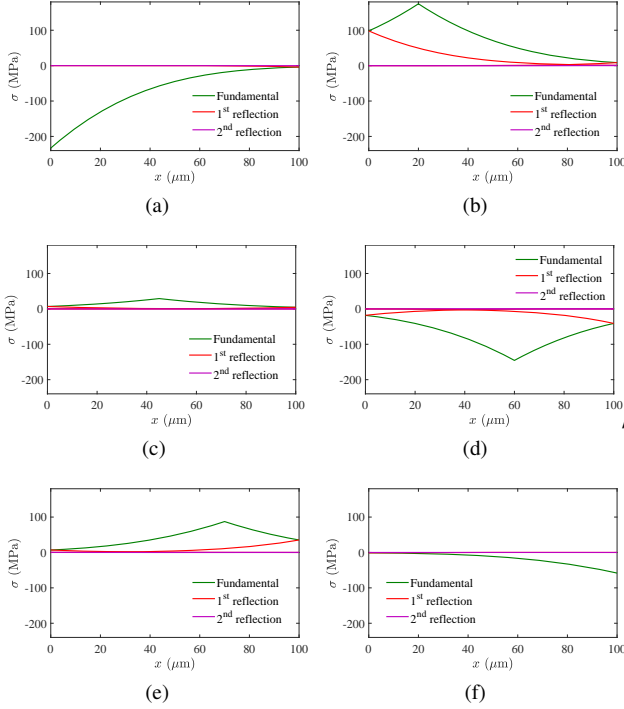


Figure 6: Stress along the five-segment interconnect for $t = 20y$ due to sources at (a) $x = 0$ (b) $x = L_1 = 20\mu\text{m}$ (c) $x = L_2 = 45\mu\text{m}$ (d) $x = L_3 = 60\mu\text{m}$ (e) $x = L_4 = 70\mu\text{m}$ (f) $x = L_5 = 100\mu\text{m}$.

is negligible. The first reflection for intermediate points in (b)–(e) is more substantial than that of the boundaries, but again, the second reflection is quite small.

We superpose these stress components to obtain stress profile at various time points. Only a few significant reflections are sufficient to build up the stress profile along the line, as shown in Fig. 7(a), where a comparison with COMSOL simulation shows a visually perfect match. The error, relative to the critical stress of 41 MPa, is quantified in Fig. 7(b) along the line and is found to be well below 0.5%.

To illustrate the termination criterion (18), for each source (at the two ends, $x = 0$ and $x = L_5$, and at intermediate L_i , going to the left (IL) and right (IR)), we show the relative attenuation in Table IV. The table shows the ratio \mathcal{R}_k of the maximum stress, $\sigma^{(k)}$, at the k^{th} reflection point to the maximum stress, $\sigma^{(0)}$, of the fundamental (at the stress source). The highest and lowest magnitudes of all reflections are at the side boundaries, $x = 0$ and $x = L_5$. For a given line, by precalculating the magnitudes at the boundaries, the order of reflections needed to reach desired accuracy can be set.

We choose the threshold $\alpha = 0.1\%$ in (18). The table shows, in boldface, the reflection at which the stress magnitude first falls below the threshold. We see that the ratio \mathcal{R}_2 for the first reflection is below α for 6 out of 10 stress components, i.e. it is enough to consider just the first reflection. For the remaining four, the ratio \mathcal{R}_3 falls below the threshold, showing that two reflections are enough for this testcase.

B. Analysis on OpenROAD power grid benchmarks

Next, we show simulations based on power grids from OpenROAD circuits designed using a commercial 12nm FinFET, commercial 28nm FDSOI, and open source FreePDK45nm with the Nangate Open Cell Library [23] using Cu DD interconnects. The circuits are taken through synthesis, placement and routing in these technology nodes (some circuits are implemented in multiple nodes) using a standard design flow. The power grid is synthesized using an open-source tool, OpenNPDN [21] from OpenROAD [23]. The IR drop and current densities per segment are computed using pdnSim [24].

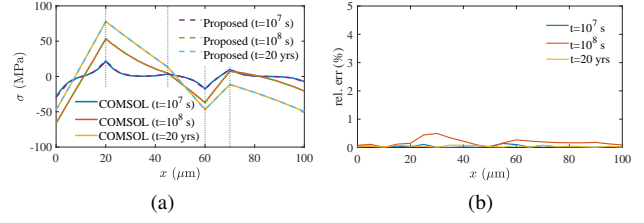


Figure 7: (a) Comparison, against COMSOL, of the results of superposing the stress waveforms from the six stress sources, shown in Fig. 6, truncated using terminating criterion $\alpha = 0.1\%$. The segment boundaries are marked by the vertical dotted lines. (b) The percentage error in estimating stress using $\alpha = 0.1\%$.

Table IV: Terminating Criterion: Ratio \mathcal{R}_k of the highest magnitude of the k^{th} reflection to the highest magnitude of the fundamental, for all stress sources on the five-segment line ($t = 20$ years)

x	0	L_1		L_2		L_3		L_4		L_5
		IL/IR	IL/IR	IL/IR	IL/IR	IL/IR	IL/IR			
\mathcal{R}_1	1.7%	56.2% / 4.9%	23.4% / 15.6%	12.6% / 28.3%	8.0% / <40.5%	1.7%				
\mathcal{R}_2	<0.1%	0.5% / <0.1%	0.5% / <0.1%	<0.1% / 0.1%	<0.1% / 0.3%	<0.1%				
\mathcal{R}_3	-	<0.1% / -	<0.1% / -	- / <0.1%	- / <0.1%	-				

All our experiments on these circuits are in Python 3.7 and performed on a 2.20 GHz Intel[®] Xeon[®] Silver 4114 CPU. A two-stage filtering process is used to reduce the number of wires needed for transient EM stress analysis:

- In the first stage, we calculate the steady-state stress, and if this is lower than the critical stress, then the wire-segment is immortal or EM-safe (EM-s) and needs not be considered further. The Blech criterion [1] has often been applied for this by multiplying each segment current density j by its length l , and comparing this against a threshold. However, this is known to be inaccurate for multisegment wires [11], [12], and we use the method of [12].
- In the second stage, we perform transient analysis for the remaining wire-segments, which are potentially mortal or EM-vulnerable (EM-v). If the stress on these wire-segments exceeds the critical stress at the specified product lifetime, then these wire-segments are in danger of EM failures (EM-f).

For the first stage, we apply the method in [12] to each layer to find the steady-state stress in linear time, which is then used to locate the potential void locations and thus segregate the EM-safe wire-segments from EM-vulnerable wire-segments. For the second stage, it is not necessary to calculate the transient-stress inside the wire-segments marked as EM-safe in the first stage. Our analytical framework is very helpful here because it can provide the closed-form solution at any location x , without evaluating all locations/segments (in contrast to a numerical FEM method which needs to perform transient analysis at all spatial discrete points). This reduces, by a large margin, the number of wire-segments that need further investigation to check the risk of EM-failure in the product lifetime.

The results of this two-stage analysis on the OpenROAD benchmarks are summarized in Table V. For each benchmark, we show the number of edges; the results of steady-state analysis, showing the number of immortal wires; the number of EM failures for product lifetimes of 5, 10, and 20 years; and the runtimes of the method. We emphasize that steady-state analysis is fast and is important in reducing the number of wires to be considered for transient analysis, but is not a contribution of this paper. Therefore, our runtime numbers focus on the time required by our reflection-based method. The runtimes shown in the last column are practically identical for all chip lifetimes, since the only extra cost when lifetime increases is the possible evaluation and addition of more reflection terms. In contrast, the runtime of an (already much slower) numerical method increases at least linearly with the time period needed for simulation.

Table V: Summary results of EM failure analysis on OpenROAD benchmarks across three process technologies

Tech	design	#segments	Steady-State		t=5yrs	t=10yrs	t=20yrs	Run times (s)
			EM-s	EM-v	EM-f	EM-f	EM-f	
12 nm	gcd	4,169	3,940	229	54	79	229	2
	aes	195,353	117,404	77,949	4	153	988	75
	dynamic_node	151,568	94,707	56,861	2	15	160	62
	jpeg	84,187	41,506	42,681	30	146	676	34
28nm	gcd	978	920	58	45	46	52	1
	aes	17,713	10,649	7,064	2	8	315	4
	jpeg	191,428	125,361	66,067	8	29	14	70
45nm	aes	8,012	4,354	3,658	3	694	1,855	2
	dynamic_node	6,614	3,302	3,312	7	501	1,013	2
	ibex	12,728	6,509	6,219	4	247	1,563	4
	swerv	61,961	43,295	18,666	5	8	12	16

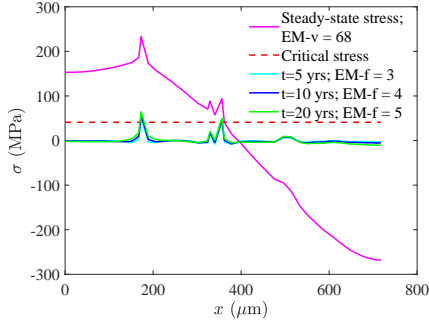


Figure 8: Stress profile of a 133-segment line of length $718\mu\text{m}$ from the jpeg benchmark, using a commercial 12nm FinFET technology.

The table shows that, as expected, the immortality filter marks a number of lines as EM-safe. EM effects are known to deteriorate over time and the table shows this trend: the number of EM-f segments increases monotonically as the product lifetime is increased. Our runtimes are extremely fast, even faster than [12], where immortality checks on these benchmarks require a few minutes.

Fig. 8 shows the stress profile along a power grid stripe in the jpeg design, implemented in a commercial 12nm technology. The $718\mu\text{m}$ long stripe contains 133 segments. The steady-state plot shows that 68 segments to the left of $x \sim 400\mu\text{m}$ exceed critical stress (the dotted line), and are EM-vulnerable. Our transient analysis confirms that (a) the EM-safe segments remain below critical stress, and (b) only 3, 4, and 5 of the 68 EM-vulnerable segments experience EM failures after 5, 10, and 20 years, respectively.

Runtime comparisons: COMSOL simulation accuracy for this stripe depends on its spatiotemporal discretization. For a 20y lifetime, COMSOL requires 7s for lower accuracy ($30\times$ slower than our method) and 8m for high accuracy ($2000\times$ slower than our method).

V. CONCLUSION

We present a general analytical method for computing the EM-induced stress in any N -segment interconnect lines. We focus on lines because (1) in modern designs, interconnects are laid out as metal lines on each layer, and (2) EM phenomena in each such line can be independently analyzed since the barrier layer in a Cu DD interconnect acts as a blocking boundary for mass transfer. Our approach provides a physical interpretation for the solution that aids both in creating a solution with generalized expressions, and in terminating our infinite series solution to a desired accuracy.

APPENDIX: PROOF DETAILS

In this section, we derive solutions to the Korhonen equation for various lines. In the following, we will denote the Laplace transform of $\sigma(x, t)$ as $\hat{\sigma}(x, s) \triangleq \int_0^{+\infty} e^{-st} \sigma(x, t) dt$. We begin by showing the machinery required to obtain the solution (6) to Korhonen's equation for a semi-infinite line, and then use it to consider the solutions to

finite lines. As we will see, the results thus obtained have a different form from the solutions in [6], and we explain in Section III how this solution can be used to achieve better physical insight into the solution that aids convergence. Taking the Laplace transform in both sides of the Korhonen equation (1), and assuming zero initial stress $\sigma(x, 0) = 0$, we obtain the ordinary differential equation:

$$\frac{d^2 \hat{\sigma}(x, s)}{dx^2} - \frac{s}{\kappa} \hat{\sigma}(x, s) = 0 \quad (19)$$

whose general solution is:

$$\hat{\sigma}(x, s) = Ae^{\sqrt{\frac{s}{\kappa}}x} + Be^{-\sqrt{\frac{s}{\kappa}}x} \quad (20)$$

The Laplace transform of the blocking boundary conditions (2) is:

$$\frac{d\hat{\sigma}(0, s)}{dx} = -\frac{G}{s}; \quad \frac{d\hat{\sigma}(L, s)}{dx} = -\frac{G}{s} \quad (21)$$

We now introduce the inverse Laplace transform [25] that we will use several times in the succeeding discussion:

$$\mathcal{L}^{-1} \left(\frac{1}{s} \sqrt{\frac{\kappa}{s}} e^{-\sqrt{\frac{s}{\kappa}}x} \right) = 2\sqrt{\frac{\kappa t}{\pi}} e^{-\frac{x^2}{4\kappa t}} - x \operatorname{erfc} \left(\frac{x}{2\sqrt{\kappa t}} \right), \quad (22)$$

$\operatorname{erfc}(x) = \frac{2}{\sqrt{\pi}} \int_x^{\infty} e^{-t^2} dt$ is the complementary error function. **Semi-infinite line** $0 < x < +\infty$. For the semi-infinite line from $x = 0$ to $+\infty$, since the stress must be bounded for $x \rightarrow +\infty$, $A = 0$ in (20). Applying the first boundary condition in (21),

$$\hat{\sigma}(x, s) = \frac{G}{s} \sqrt{\frac{\kappa}{s}} e^{-\sqrt{\frac{s}{\kappa}}x} \quad (23)$$

Applying the inverse Laplace transform (22) we obtain:

$$\sigma(x, t) = G \left(2\sqrt{\frac{\kappa t}{\pi}} e^{-\frac{x^2}{4\kappa t}} - x \operatorname{erfc} \left(\frac{x}{2\sqrt{\kappa t}} \right) \right) \quad (24)$$

which is the solution given originally in [6].

Semi-infinite line $-\infty < x < L$. For the semi-infinite line from L to $-\infty$, to ensure bounded stress as $x \rightarrow -\infty$, we must have $B = 0$ in (20). Applying the second boundary condition in (21),

$$\hat{\sigma}(x, s) = -\frac{G}{s} \sqrt{\frac{\kappa}{s}} e^{-\sqrt{\frac{s}{\kappa}}(L-x)} \quad (25)$$

An inverse Laplace transform using (22) yields the solution:

$$\sigma(x, t) = -G \left(2\sqrt{\frac{\kappa t}{\pi}} e^{-\frac{(L-x)^2}{4\kappa t}} - (L-x) \operatorname{erfc} \left(\frac{L-x}{2\sqrt{\kappa t}} \right) \right) \quad (26)$$

Finite line $0 < x < L$. For the single-segment finite line from 0 to L we apply boundary conditions (21) to the general solution (20), whereby solving with respect to parameters A, B we have:

$$A = \frac{G}{s} \sqrt{\frac{\kappa}{s}} \frac{e^{-\sqrt{\frac{s}{\kappa}}L} - 1}{e^{\sqrt{\frac{s}{\kappa}}L} - e^{-\sqrt{\frac{s}{\kappa}}L}}, \quad B = \frac{G}{s} \sqrt{\frac{\kappa}{s}} \frac{e^{\sqrt{\frac{s}{\kappa}}L} - 1}{e^{\sqrt{\frac{s}{\kappa}}L} - e^{-\sqrt{\frac{s}{\kappa}}L}}$$

Then after some algebraic manipulations, (20) becomes:

$$\begin{aligned} \hat{\sigma}(x, s) &= \frac{G}{s} \sqrt{\frac{\kappa}{s}} \left[\frac{(e^{-\sqrt{\frac{s}{\kappa}}L} - 1) e^{\sqrt{\frac{s}{\kappa}}x} + (e^{\sqrt{\frac{s}{\kappa}}L} - 1) e^{-\sqrt{\frac{s}{\kappa}}x}}{e^{\sqrt{\frac{s}{\kappa}}L} - e^{-\sqrt{\frac{s}{\kappa}}L}} \right] \\ &= \frac{G}{s} \sqrt{\frac{\kappa}{s}} \left[\frac{e^{-\sqrt{\frac{s}{\kappa}}(L-x)} - e^{\sqrt{\frac{s}{\kappa}}x} + e^{\sqrt{\frac{s}{\kappa}}(L-x)} - e^{-\sqrt{\frac{s}{\kappa}}x}}{e^{\sqrt{\frac{s}{\kappa}}L} - e^{-\sqrt{\frac{s}{\kappa}}L}} \right] \\ &= \frac{G}{s} \sqrt{\frac{\kappa}{s}} \left[\frac{2 \left(\cosh \left(\sqrt{\frac{s}{\kappa}}(L-x) \right) - \cosh \left(\sqrt{\frac{s}{\kappa}}x \right) \right)}{2 \sinh \left(\sqrt{\frac{s}{\kappa}}L \right)} \right] \\ &= \frac{G}{s} \sqrt{\frac{\kappa}{s}} \left[\frac{2 \sinh \left(\sqrt{\frac{s}{\kappa}} \frac{L}{2} \right) \sinh \left(\sqrt{\frac{s}{\kappa}} \frac{L-2x}{2} \right)}{2 \sinh \left(\sqrt{\frac{s}{\kappa}} \frac{L}{2} \right) \cosh \left(\sqrt{\frac{s}{\kappa}} \frac{L}{2} \right)} \right] \end{aligned}$$

$$\begin{aligned}
&= \frac{G}{s} \sqrt{\frac{\kappa}{s}} \left[\frac{e^{\sqrt{\frac{s}{\kappa}} \frac{L-2x}{2}} - e^{-\sqrt{\frac{s}{\kappa}} \frac{L-2x}{2}}}{e^{\sqrt{\frac{s}{\kappa}} \frac{L}{2}} + e^{-\sqrt{\frac{s}{\kappa}} \frac{L}{2}}} \right] \\
&= \frac{G}{s} \sqrt{\frac{\kappa}{s}} \left[\frac{e^{\sqrt{\frac{s}{\kappa}} \frac{L-2x}{2}} - e^{-\sqrt{\frac{s}{\kappa}} \frac{L-2x}{2}}}{1 + e^{-\sqrt{\frac{s}{\kappa}} L}} e^{-\sqrt{\frac{s}{\kappa}} \frac{L}{2}} \right] \\
&= \frac{G}{s} \sqrt{\frac{\kappa}{s}} \left[\frac{e^{-\sqrt{\frac{s}{\kappa}} x} - e^{-\sqrt{\frac{s}{\kappa}} (L-x)}}{1 + e^{-\sqrt{\frac{s}{\kappa}} L}} \right]
\end{aligned}$$

We now use the binomial expansion

$$(1 + e^{-\sqrt{\frac{s}{\kappa}} L})^{-1} = \sum_{n=0}^{\infty} (-1)^n e^{-\sqrt{\frac{s}{\kappa}} nL}$$

to arrive at the infinite series representation of the solution:

$$\hat{\sigma}(x, s) = \frac{G}{s} \sqrt{\frac{\kappa}{s}} \sum_{n=0}^{\infty} (-1)^n \left(e^{-\sqrt{\frac{s}{\kappa}} (nL+x)} - e^{-\sqrt{\frac{s}{\kappa}} ((n+1)L-x)} \right) \quad (27)$$

With the inverse Laplace transform, the time-domain solution is:

$$\begin{aligned}
\sigma(x, t) = G \sum_{n=0}^{\infty} (-1)^n &\left[2\sqrt{\frac{\kappa t}{\pi}} e^{-\frac{(nL+x)^2}{4\kappa t}} - (nL+x) \operatorname{erfc} \frac{nL+x}{2\sqrt{\kappa t}} \right. \\
&\left. - 2\sqrt{\frac{\kappa t}{\pi}} e^{-\frac{((n+1)L-x)^2}{4\kappa t}} + ((n+1)L-x) \operatorname{erfc} \frac{(n+1)L-x}{2\sqrt{\kappa t}} \right] \quad (28)
\end{aligned}$$

The solution (28) is a different infinite series solution than the one given in [6]. The series (28) is directly comparable to the semi-infinite line solutions (24) and (26), and its terms include these fundamental semi-infinite solutions as well as their successive reflections at the physical boundaries (as remarked in Section III).

Infinite composite line ($-\infty < x < L_1$) \wedge ($L_1 < x < +\infty$). The two-segment infinite line with intersection at $x = L_1$ can be considered to be a composite of two semi-infinite lines, each with different parameters G_1 and G_2 (corresponding to their different electron current densities) and different stresses $\sigma_1(x, t)$ and $\sigma_2(x, t)$ in each of the two semi-infinite segments.

However, they must obey additional boundary conditions beyond those for the semi-infinite lines discussed earlier, which enforce continuous atomic flux (4), and continuous stress (5) at the intersection. The boundary conditions are transformed in the Laplace domain as:

$$\frac{d\hat{\sigma}_1(L_1, s)}{dx} + \frac{G_1}{s} = \frac{d\hat{\sigma}_2(L_1, s)}{dx} + \frac{G_2}{s} \quad (29)$$

$$\hat{\sigma}_1(L_1, s) = \hat{\sigma}_2(L_1, s) \quad (30)$$

As before, to avoid unbounded stresses at $\pm\infty$, the Laplace-domain stresses $\hat{\sigma}_1(x, s)$ and $\hat{\sigma}_2(x, s)$ in the segments $-\infty < x < L_1$ and $L_1 < x < +\infty$ will have, respectively, $B = 0$ and $A = 0$ in (20). Applying the boundary conditions (29) and (30) we obtain:

$$\hat{\sigma}_1(x, s) = \frac{G_2 - G_1}{2s} \sqrt{\frac{\kappa}{s}} e^{-\sqrt{\frac{s}{\kappa}} (L_1-x)}$$

$$\hat{\sigma}_2(x, s) = \frac{G_2 - G_1}{2s} \sqrt{\frac{\kappa}{s}} e^{-\sqrt{\frac{s}{\kappa}} (x-L_1)}$$

Taking the inverse Laplace transform we finally arrive at the time-domain solution for the two-segment infinite line:

$$\sigma_1(x, t) = \frac{G_2 - G_1}{2} \left(2\sqrt{\frac{\kappa t}{\pi}} e^{-\frac{(L_1-x)^2}{4\kappa t}} - (L_1-x) \operatorname{erfc} \left(\frac{L_1-x}{2\sqrt{\kappa t}} \right) \right) \quad (31)$$

$$\sigma_2(x, t) = \frac{G_2 - G_1}{2} \left(2\sqrt{\frac{\kappa t}{\pi}} e^{-\frac{(x-L_1)^2}{4\kappa t}} - (x-L_1) \operatorname{erfc} \left(\frac{x-L_1}{2\sqrt{\kappa t}} \right) \right) \quad (32)$$

REFERENCES

- [1] I. A. Blech, "Electromigration in thin aluminum films on titanium nitride," *J. Appl. Phys.*, vol. 47, no. 4, pp. 1203–1208, 1976.
- [2] J. R. Black, "Electromigration failure modes in aluminum metallization for semiconductor devices," *Proc. IEEE*, vol. 57, no. 9, pp. 1587–1594, 1969.
- [3] R. Rosenberg and M. Ohring, "Void formation and growth during electromigration in thin films," *J. Appl. Phys.*, vol. 42, no. 13, pp. 5671–5679, 1971.
- [4] M. Schatzkes and J. R. Lloyd, "A model for conductor failure considering diffusion concurrently with electromigration resulting in a current exponent of 2," *J. Appl. Phys.*, vol. 59, pp. 3890–3893, 1986.
- [5] J. J. Clement and J. R. Lloyd, "Numerical investigations of the electromigration boundary value problem," *J. Appl. Phys.*, vol. 71, pp. 1729–1731, 1992.
- [6] M. A. Korhonen, *et al.*, "Stress evolution due to electromigration in confined metal lines," *J. Appl. Phys.*, vol. 73, no. 8, pp. 3790–3799, 1993.
- [7] V. Sukharev, "Beyond Black's equation: Full-chip EM/SM assessment in 3D IC stack," *Microelectronic Engineering*, vol. 120, pp. 99–105, 2014.
- [8] V. Mishra and S. S. Sapatnekar, "The impact of electromigration in copper interconnects on power grid integrity," in *Proc. DAC*, pp. 88:1–88:6, 2013.
- [9] H. Haznedar, *et al.*, "Impact of stress-induced backflow on full-chip electromigration risk assessment," *IEEE T. Comput. Aid D.*, vol. 25, pp. 1038–1046, June 2006.
- [10] V. Mishra and S. S. Sapatnekar, "Predicting electromigration mortality under temperature and product lifetime specifications," in *Proc. DAC*, pp. 43:1–43:6, 2016.
- [11] Z. Sun, *et al.*, "Fast electromigration immortality analysis for multi-segment copper interconnect wires," *IEEE T. Comput. Aid D.*, vol. 37, pp. 3137–3150, Dec. 2018.
- [12] M. A. A. Shohel, *et al.*, "A new, computationally efficient "Blech criterion" for immortality in general interconnects," in *Proc. DAC*, 2021. (to appear; available at <https://arxiv.org/abs/2105.08784>).
- [13] H.-B. Chen, *et al.*, "Analytical modeling and characterization of electromigration effects for multibranch interconnect trees," *IEEE T. Comput. Aid D.*, vol. 35, no. 11, pp. 1811–1824, 2016.
- [14] H.-B. Chen, *et al.*, "Analytical modeling of electromigration failure for VLSI interconnect tree considering temperature and segment length effects," *IEEE T. Device Mater. Rel.*, vol. 17, no. 4, pp. 653–666, 2017.
- [15] S. Chatterjee, *et al.*, "Power grid electromigration checking using physics-based models," *IEEE T. Comput. Aid D.*, vol. 37, pp. 1317–1330, July 2018.
- [16] J. Gambino, "Process technology for copper interconnects," in *Handbook of Thin Film Deposition* (K. Seshan and D. Schepis, eds.), ch. 6, pp. 147–194, Amsterdam, The Netherlands: Elsevier, 3rd ed., 2018.
- [17] L. Zhang, *et al.*, "Grain size and cap layer effects on electromigration reliability of cu interconnects: Experiments and simulation," in *AIP Conf. Proc.*, vol. 1300, 3, 2010.
- [18] N. Pande, *et al.*, "Characterizing electromigration effects in a 16nm FinFET process using a circuit based test vehicle," in *Proc. IEDM*, pp. 5.3.1–5.3.4, 2019.
- [19] C. Chan, *et al.*, "Integrated circuit design incorporating a power mesh," Nov. 12 2002. US Patent 6,480,989 B2.
- [20] W. Chang, *et al.*, "Practical routability-driven design flow for multilayer power networks using aluminum-pad layer," *IEEE T. VLSI Syst.*, vol. 22, no. 5, pp. 1069–1081, 2014.
- [21] V. A. Chhabria, *et al.*, "Template-based PDN synthesis in floorplan and placement using classifier and CNN techniques," in *Proc. ASP-DAC*, pp. 44–49, 2020.
- [22] S. M. Alam, *et al.*, "Circuit-level reliability requirements for Cu metallization," *IEEE T. Device Mater. Rel.*, vol. 5, no. 3, pp. 522–531, 2005.
- [23] "The OpenROAD project." github.com/The-OpenROAD-Project.
- [24] "PDNSim." <https://github.com/The-OpenROAD-Project/OpenROAD/tree/master/src/PDNSim>.
- [25] A. Erdélyi, ed., *Tables of Integral Transforms*. New York, NY: McGraw-Hill, 1954.